Journal of Biomedical Optics

SPIEDigitalLibrary.org/jbo

Reducing motion artifacts in photoplethysmograms by using relative sensor motion: phantom study

Ralph W. C. G. R. Wijshoff
Massimo Mischi
Jeroen Veen
Alexander M. van der Lee
Ronald M. Aarts

SPIE

Reducing motion artifacts in photoplethysmograms by using relative sensor motion: phantom study

Ralph W. C. G. R. Wijshoff,[a] Massimo Mischi,[a] Jeroen Veen,[b] Alexander M. van der Lee,[c] and Ronald M. Aarts[a,d]
[a]Eindhoven University of Technology, Department of Electrical Engineering, Signal Processing Systems, Den Dolech 2, 5612 AZ Eindhoven, the Netherlands
[b]Philips Research, Patient Care Solutions, High Tech Campus 34, 5656 AE Eindhoven, the Netherlands
[c]Philips Research, Light Generation, High Tech Campus 4, 5656 AE Eindhoven, the Netherlands
[d]Philips Research, Digital Signal Processing, High Tech Campus 36, 5656 AE Eindhoven, the Netherlands

Abstract. Currently, photoplethysmograms (PPGs) are mostly used to determine a patient's blood oxygenation and pulse rate. However, PPG morphology conveys more information about the patient's cardiovascular status. Extracting this information requires measuring clean PPG waveforms that are free of artifacts. PPGs are highly susceptible to motion, which can distort the PPG-derived data. Part of the motion artifacts are considered to result from sensor-tissue motion and sensor deformation. It is hypothesized that these motion artifacts correlate with movement of the sensor with respect to the skin. This hypothesis has been proven true in a laboratory setup. *In vitro* PPGs have been measured in a skin perfusion phantom that is illuminated by a laser diode. Optical motion artifacts are generated in the PPG by translating the laser diode with respect to the PPG photodiode. The optical motion artifacts have been reduced significantly *in vitro*, by using a normalized least-mean-square algorithm with only a single coefficient that uses the laser's displacement as a reference for the motion artifacts. Laser displacement has been measured accurately via self-mixing interferometry by a compact laser diode with a ball lens integrated into the package, which can be easily integrated into a commercial sensor. [DOI: 10.1117/1.JBO.17.11.117007]

Keywords: correlation cancellation; interferometry; motion artifact; photoplethysmography; pulse oximetry.

Paper 12390P received Jun. 22, 2012; revised manuscript received Sep. 23, 2012; accepted for publication Oct. 25, 2012; published online Nov. 29, 2012.

1 Introduction

Pulse oximeters are currently widely applied in clinical practice to measure a patient's peripheral arterial oxygen saturation (SpO_2) and pulse rate (PR).[1] Pulse oximeters derive these data from photoplethysmograms (PPGs). PPGs are obtained by illuminating the skin and measuring the intensity of the light that has propagated through the skin in a transmissive or planar configuration, the latter being referred to as a reflective PPG sensor. A transmissive finger sensor is illustrated schematically in Fig. 1. Reflective sensors are for instance used on a patient's forehead. PPGs show periodic decreases as a result of cardiac induced increases in tissue arterial blood volume [first 10 s and last 12 s in Fig. 2(a), and the first 23 s in Fig. 2(b)]. PR can be directly obtained using this periodicity.[2] By measuring two PPGs at different wavelengths, commonly red and infrared, SpO_2 can be determined. Because blood oxygen saturation determines the blood's color, SpO_2 can be determined from the ratio of the DC-normalized amplitudes of the cardiac induced pulses in both PPGs.[3]

This paper focuses on the use of reflective PPG sensors, which are potentially more widely applicable than transmissive sensors, as reflective sensors are not restricted to transilluminable body sites.[4] On central sites, such as the forehead, reflective sensors have been shown to measure desaturation events earlier than finger sensors as a result of a shorter circulation transit time.[5,6] Also, PPG measurements on the forehead suffer to a lesser extent from vasoconstrictive responses[5] and motion artifacts.[7]

Though in clinical practice PPGs are mostly used to measure SpO_2 and PR, their morphology conveys rich information about the patient's cardiovascular status,[8] sympathetic tone[9–11] and respiration.[4,9,12,13] Additionally, heart rate variability (HRV) can be determined from PPGs,[13,14] and the arrival or transit time of the cardiac induced pulses in PPGs can be used to monitor changes in blood pressure or arterial compliance.[4,10] Furthermore, PPGs are highly susceptible to patient and sensor-tissue motion, which can distort PPGs and derived data.[1,4,13,15] This is illustrated in Fig. 2(a) and 2(b), which show motion artifacts in finger PPGs as a result of finger bending and motion artifacts in forehead PPGs as a result of walking, respectively. Therefore, to enable reliable extraction of beat-to-beat information from PPG morphology, an improved PPG motion artifact reduction is required which cleans up the PPG waveform.

Current commercial algorithms have mainly been designed to extract average SpO_2 and PR and do not use an explicit measurement of motion to reduce the motion artifacts in the PPGs, such as the Philips FAST-SpO_2 algorithm[16,17] or the Masimo SET® algorithm.[18,19] Also in scientific literature, several different approaches to reduce motion artifacts in PPGs have been investigated. The main approaches are illustrated in the following examples. For a ring-shaped PPG sensor that measures transmissive and reflective PPGs, the reflective PPG has been suggested as a reference for the motion artifacts to clean up

Address all correspondence to: Ralph Wijshoff, Eindhoven University of Technology, Department of Electrical Engineering, Signal Processing Systems, Den Dolech 2, 5612 AZ Eindhoven, the Netherlands. Tel: +31 40 274 7821; Fax: +31 40 246 6508; E-mail: R.W.C.G.R.Wijshoff@tue.nl

0091-3286/2012/$25.00 © 2012 SPIE

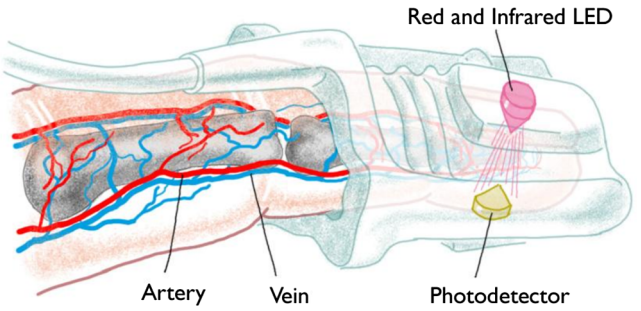

Fig. 1 Schematic of a transmissive finger pulse oximetry clip.

the transmissive PPG.[20] In an earpiece PPG sensor, a notch filter at the motion frequency removed the motion artifacts from the PPGs. The motion frequency was determined from the photodiode signal with the light emitting diodes (LEDs) switched off, as sensor-tissue motion caused a variation in the amount of ambient light reaching the photodiode.[21] Accelerometers have been applied as well to obtain a reference for the motion artifacts in a correlation canceler,[22] also combined with the Laguerre expansion.[23] Furthermore, sensor-coupling motion artifacts have been removed by equalizing a transmissive PPG by a second transmissive PPG measured at a different wavelength.[24] Lastly, the influence of motion on SpO_2 measurements can be reduced by using wavelets,[25] the smoothed pseudo Wigner-Ville distribution,[26] and multiple colors.[27]

In this paper, a motion artifact reduction method is proposed to clean up the PPG, in order to enable reliable extraction of beat-to-beat information from the PPG waveform. Different from other methods, the proposed method is based on the use of relative sensor motion with respect to the skin as a reference for the motion artifacts.[28] Motion artifacts in PPGs are presumably caused by hemodynamic effects, tissue deformation, and sensor movement and deformation.[1,2,4,24] It is hypothesized that a large part of these motion artifacts correlate with relative sensor motion. When the sensor moves with respect to the skin, spurious fluctuations occur in the PPG as a result of variations in light coupling and the probed tissue volume, e.g., changes in the shunt light which does not probe pulsatile blood volume.[2,24] It is expected that an estimate of these motion artifacts can be derived from a measure of relative sensor motion in order to remove these artifacts from the PPGs. Moreover, by deriving motion artifacts from relative sensor motion, one can possibly obtain insight in the relative contribution of these artifacts to the total artifact that results from motion.

We propose to measure relative sensor motion via self-mixing interferometry (SMI). This can be done by integrating a laser diode with a monitor diode into a PPG sensor such that the laser diode illuminates the skin. When the sensor moves with respect to the skin and the backscattered laser light re-enters the laser cavity, its Doppler shift can be determined via the monitor diode. Relative sensor motion can subsequently be determined from the Doppler phase, as explained in Sec. 2.1. Using SMI is practical, because this method is self-aligning, compact, and easy to integrate in a PPG sensor. As described in Sec. 2.2, we use an *in vitro* skin perfusion phantom in a laboratory setup to develop a method to measure relative motion via SMI, and to investigate the influence of sensor motion on PPGs. In this setup, a single laser diode is used both as a light source for the PPG measurements and as a sensor to measure displacement. Optical motion artifacts are generated in the setup by translating the laser diode with respect to the PPG photodiode. Last, the SMI displacement measurement is used as a reference for the motion artifacts in a normalized least-mean-square (NLMS) algorithm,[29] as described in Sec. 2.3. In this algorithm, an estimate of the motion artifacts derived from the SMI displacement measurement is subtracted from the distorted *in vitro* PPG to reduce the motion artifacts and to retrieve the mimicked cardiac component. The accuracy of the SMI displacement measurement, the *in vitro* PPGs obtained and the performance of the artifact reduction are presented and discussed in Secs. 3 and 4, respectively, and conclusions are presented in Sec. 5.

2 Methodology

2.1 *Self-Mixing Interferometry*

SMI is observed when a laser diode illuminates an object such that part of the light backscattered by the object re-enters the laser diode's cavity. The backscattered light interferes with the standing wave inside the laser cavity, thus changing the emitted optical lasing frequency and power.[30] Moreover, when light re-enters the cavity that has been backscattered by a moving object, a beat frequency $f_d(t)$ [Hz] equal to the Doppler shift is observed in the optical power:

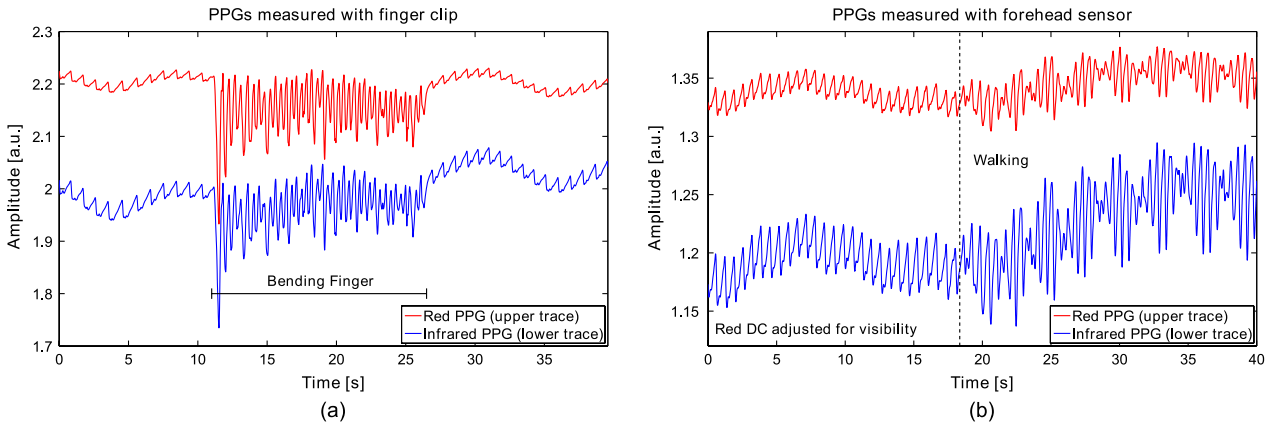

Fig. 2 Illustration of the effect of motion on PPGs. (a) PPGs obtained using a transmissive finger clip. The motion artifacts are caused by repetitive slight bending of the finger. (b) PPGs obtained using a reflective forehead sensor. Walking causes the motion artifacts.

$$f_d(t) = \frac{v_o(t)\cos(\theta)}{\lambda(t)/2}, \tag{1}$$

with time t [s], object velocity $v_o(t)$ [m/s], angle θ [rad] between the object's velocity vector and the laser beam, and lasing wavelength $\lambda(t)$ [m]. The component of the object's displacement in the direction of the laser beam follows by equating each full cycle in the optical power to half of the emitted wavelength.

However, only counting the number of cycles in the optical power does not reveal the direction of motion, because in this case one uses the absolute value of the object's velocity. Without directional information, the displacement measurement can have a frequency twice as high as the displacement itself (frequency doubling as a result of using the absolute value of the velocity). This complicates its use to correct PPG motion artifacts which are caused by variations in sensor position. Therefore, displacement should be measured such that the direction is taken into account as well. Note that with a single laser diode, one can only determine whether the net motion in three dimensions is directed towards or away from the laser beam. Because the three-dimensional motion is projected onto a single axis only, it is not possible to determine the exact direction of motion in three-dimensional space. Moreover, any motion orthogonal to the laser beam is not observed at all. These can be limitations of the current configuration.

When using SMI, the direction of motion can be determined either from the shape of the interference pattern in the optical power, or by modulating the emitted wavelength. At moderate levels of optical feedback, the interference pattern is sawtooth shaped. In this case the direction of motion determines whether the fast edge of the sawtooth is directed upwards or downwards.[31–33] However, if the direction of motion is determined from the fast edge of the sawtooth shaped interference pattern, the level of optical feedback is required to exceed some threshold to guarantee proper functioning of the displacement measuring method. That is, sawtooth-shaped interference patterns are only observed at moderate levels of optical feedback; at (very) weak levels of optical feedback the interference pattern is sinusoidally shaped. In this application though, the level of optical feedback can be (very) weak, thus not exceeding the required threshold to obtain sawtooth shaped interference patterns. This is because the level of optical feedback is linearly related to both the reflectivity of the illuminated object and the distance from the laser diode to the object.[30–33] Because skin diffusely scatters the light and because the optical properties of skin are highly variable, in some conditions weak backscattering from the skin can lead to (very) weak optical feedback. In addition, the distance between the skin and the laser diode will only be on the order of millimeters. For these reasons, we prefer to use a method that can also observe the direction of motion at (very) weak feedback levels. This is accomplished by amplitude modulation of the laser injection current, which induces a wavelength modulation. In this case the direction of motion can be recovered by using two spectral Doppler components of the SMI signal, as explained in the next sections. The structure of the SMI signal is first explained in Sec. 2.1.1. Next, Sec. 2.1.2 explains how displacement is determined from the SMI signal. And finally, the accuracy of the obtained displacement measurement is described in Sec. 2.1.3.

2.1.1 *SMI signal structure*

The Doppler frequency in the optical power can be measured by the laser diode's internal monitor diode. The monitor signal $v_{\mathrm{MD}}(t)$ [V] is obtained from the monitor diode current $i_{\mathrm{MD}}(t)$ [A] via a transimpedance amplifier with gain Z [V/A], and can be expressed as:[31–35]

$$v_{\mathrm{MD}}(t) = Zi_{\mathrm{MD}}(t) = ZR[P_{\mathrm{DC}} + \Delta P_m \sin(\omega_m t + \phi_m)] \times \{1 + m(t)\cos[\phi_{\mathrm{ext}}(t)]\}, \tag{2}$$

in which R [A/W] is the monitor diode's responsivity, P_{DC} [W] is the DC optical power, and ΔP_m [W] is the amplitude of the AC optical power as a result of the modulation of the laser injection current at ω_m [rad/s] with initial phase ϕ_m [rad]. The factor between braces describes the fluctuations in optical power caused by optical feedback. Here $m(t)$ [-] is the modulation depth which depends on the level of optical feedback. The modulation depth is assumed to be time dependent, because speckle effects cause the level of optical feedback to vary over time.[32] Last, phase $\phi_{\mathrm{ext}}(t)$ [rad] is the interferometric phase of the light that re-enters the laser cavity, which contains the object's displacement information. Because $\Delta P_m/P_{\mathrm{DC}} \ll 1$ and $m(t) < 1$, Eq. (2) can be approximated by:

$$v_{\mathrm{MD}}(t) \approx ZR\left\{P_{\mathrm{DC}} + \Delta P_m \sin(\omega_m t + \phi_m) + m(t)P_{\mathrm{DC}} \times \cos\left[\frac{4\pi L_o}{\lambda(t)} + 2\pi\int_0^t f_d(\xi)d\xi\right]\right\}, \tag{3}$$

in which the phase change of the external cavity $\phi_{\mathrm{ext}}(t)$ equals the phase change as a result of the distance L_o [m] traveled between laser diode and object, plus the Doppler phase change as a result of object motion. The amplitude modulation of the injection current results in a wavelength modulation, expressed as $\lambda_{\mathrm{mod}}(t) = \lambda_0 + \Delta\lambda_m \sin(\omega_m t + \phi_m)$. In addition, the time-varying optical feedback results in a fluctuation of the emitted wavelength, indicated by $\Delta\lambda_{\mathrm{fb}}(t)$ [m]. As $\Delta\lambda_m(t)/\lambda_0 \ll 1$ and $\Delta\lambda_{\mathrm{fb}}(t)/\lambda_0 \ll 1$, the cosine term in Eq. (3) can be approximated by:

$$\begin{aligned}\cos\left[\frac{4\pi L_o}{\lambda(t)} + 2\pi\int_0^t f_d(\xi)\mathrm{d}\xi\right] &\approx \cos\left\{\frac{4\pi L_o}{\lambda_0}\left[1 - \frac{\Delta\lambda_m}{\lambda_0}\sin(\omega_m t + \phi_m) - \frac{\Delta\lambda_{\mathrm{fb}}(t)}{\lambda_0}\right] + \frac{4\pi\cos(\theta)}{\lambda_0}\int_0^t v_o(\xi)\mathrm{d}\xi \right.\\ &\left. - \frac{8\pi\cos(\theta)}{\lambda_0}\frac{\Delta\lambda_m}{\lambda_0}\frac{v_{o\,\max}}{\omega_m} - \frac{\lambda_0}{2\pi L_o}C\right\} \end{aligned} \tag{4}$$

$$\approx \cos\left\{\frac{4\pi L_o}{\lambda_0}\left[1 - \frac{\Delta\lambda_m}{\lambda_0}\sin(\omega_m t + \phi_m) - \frac{\Delta\lambda_{\mathrm{fb}}(t)}{\lambda_0}\right] + \frac{4\pi\cos(\theta)}{\lambda_0}\int_0^t v_o(\xi)\mathrm{d}\xi\right\} \tag{5}$$

$$= \cos[\phi_d(t)]\cos[\phi_0\sin(\omega_m t + \phi_m)] + \sin[\phi_d(t)]\sin[\phi_0\sin(\omega_m t + \phi_m)], \tag{6}$$

in which:

$$\phi_d(t) = \frac{4\pi L_o}{\lambda_0}\left[1 - \frac{\Delta\lambda_{\mathrm{fb}}(t)}{\lambda_0}\right] + \frac{4\pi\cos(\theta)}{\lambda_0}\int_0^t v_o(\xi)\mathrm{d}\xi, \quad (7)$$

$$\phi_0 = \frac{4\pi L_o \Delta\lambda_m}{\lambda_0^2}. \quad (8)$$

The one but last term of the argument in Eq. (4) is the upper bound of the effect of modulation on the integral of the Doppler frequency, in which $v_{o\,\max}$ [m/s] is the maximum object velocity. The upper bound has been obtained by integrating over half of the modulation period; this term would equal zero when integrating over a full modulation period. This term is neglected in Eq. (5), because both $\Delta\lambda_m/\lambda_0 \ll 1$ and $v_{o\_\max}/\omega_m \ll 1$. Furthermore, the last term of the argument in Eq. (4) is an approximation of the effect of the feedback induced wavelength variation on the integral of the Doppler frequency, in which C [-] is the optical feedback parameter.[30,33] This approximation has been obtained by using that $\Delta\lambda_{\mathrm{fb}}(t)$ varies with the Doppler frequency, just as the light intensity in the laser cavity,[31] and integrating over half of a Doppler period. In addition, it has been used that the maximum feedback induced wavelength variation equals $\Delta\lambda_{\mathrm{fb\_max}} = \pm(\lambda_0^2 C)/(4\pi L_o)$, which has been derived from the laser phase condition that includes the effect of feedback, and by using the optical feedback parameter C.[30,33] Also this term has been neglected in Eq. (5), because $\lambda_0/L_o \ll 1$ and because $C < 1$ in the (very) weak feedback regime.[32]

Via real-valued variations of the Jacobi-Anger expansion, one can obtain a first order approximation of Eq. (6). By using the relationship $J_{-n}(z) = (-1)^n J_n(z)$ for the Bessel function of the first kind of order n, the following expression can be obtained for the Jacobi-Anger expansion:[36]

$$\begin{aligned} e^{jz\,\sin\theta} &= \sum_{n=-\infty}^{\infty} J_n(z)e^{jn\theta} \\ &= J_0(z) + 2\sum_{n=1}^{\infty} J_{2n}(z)\cos(2n\theta) \\ &\quad + 2j\sum_{n=1}^{\infty} J_{2n-1}(z)\sin[(2n-1)\theta]. \end{aligned} \quad (9)$$

By using the first order approximations of the real and imaginary parts of Eq. (9) for $\cos[\phi_0\,\sin(\omega_m t + \phi_m)]$ and $\sin[\phi_0\,\sin(\omega_m t + \phi_m)]$ in Eq. (6), respectively, and substituting this result in Eq. (3), the monitor diode signal can be expressed as a sum of signals in the baseband, around the modulation frequency, and around the second harmonic of the modulation frequency:

$$\begin{aligned} v_{\mathrm{MD}}(t) \approx ZR(&P_{\mathrm{DC}} + \Delta P_m\,\sin(\omega_m t + \phi_m) \\ &+ m(t)P_{\mathrm{DC}}\{J_0(\phi_0) + 2J_2(\phi_0)\cos[2(\omega_m t + \varphi_m)]\} \\ &\times\cos[\phi_d(t)] + 2m(t)P_{\mathrm{DC}}J_1(\phi_0) \\ &\times\sin(\omega_m t + \phi_m)\sin[\phi_d(t)]). \end{aligned} \quad (10)$$

Equation (10) shows that light backscattered into the laser cavity by a moving object yields Doppler signals with a phase $\phi_d(t)$ as in Eq. (7). As modulation causes $\phi_d(t)$ to appear both in a sine and a cosine, it can be recovered conveniently by unwrapping the arctangent of the ratio of the sine and the cosine. Moreover, Eq. (10) shows that $\cos[\phi_d(t)]$ appears both in the baseband and around the second harmonic of the modulation frequency. The $\cos[\phi_d(t)]$ term around the second harmonic is used for the displacement measurements, because it has a better SNR given the $1/f$ noise characteristic of the monitor diode and the electronics, and mains interference.

Moreover, Eq. (10) shows that the Doppler signals in the baseband, around the modulation frequency, and around the second harmonic of the modulation frequency are proportional to $J_0(\phi_0)$, $J_1(\phi_0)$ and $J_2(\phi_0)$, respectively. Therefore, a proper choice of ϕ_0 will result in Doppler signals with a large amplitude around the modulation frequency and its second harmonic, and a small amplitude in the baseband. The latter is advantageous in this study, because here the laser diode is also used to measure the PPG. By reducing the amplitude of the Doppler signals in the baseband, one improves the SNR of the PPG. The preferred ϕ_0 equals approximately 0.77π rad, at which phase $J_0(\phi_0)$ is approximately 0. As Eq. (8) shows, one can obtain the preferred ϕ_0 by adjusting modulation depth $\Delta\lambda_m/\lambda_0$, which is proportional to the AC component of the laser injection current. Moreover, Eq. (8) shows that the modulation depth required to obtain the preferred ϕ_0 depends on the distance L_o between laser diode and object. Because L_o is constant in the *in vitro* setup, the required modulation depth is not a time-varying parameter in this study. Finally, by using $\phi_0 = 0.77\pi$ rad, $L_o \sim 4$ mm, and $\lambda_0 = 850$ nm in Eq. (8), it follows that the required modulation depth is approximately $\Delta\lambda_m/\lambda_0 \sim 4 \cdot 10^{-5}$. This also confirms the validity of the assumption $\Delta\lambda_m/\lambda_0 \ll 1$.

2.1.2 *Displacement measurement*

The block diagram in Fig. 3 describes how displacement is determined from the monitor diode signal. As a first step to track the Doppler phase $\phi_d(t)$, the Doppler signals are demodulated and band-pass filtered (BPF) to obtain baseband signals:

$$\begin{aligned} v_y(t) &= 2\,\mathrm{BPF}[v_{\mathrm{MD}}(t)\sin(\omega_m t + \phi_m)] \\ &= 2ZRm(t)P_{\mathrm{DC}}J_1(\phi_0)\sin[\phi_d(t)] = A_y(t)\sin[\phi_d(t)], \end{aligned} \quad (11)$$

$$\begin{aligned} v_x(t) &= 2\,\mathrm{BPF}\{v_{\mathrm{MD}}(t)\cos[2(\omega_m t + \phi_m)]\} \\ &= 2ZRm(t)P_{\mathrm{DC}}J_2(\phi_0)\cos[\phi_d(t)] = A_x(t)\cos[\phi_d(t)], \end{aligned} \quad (12)$$

in which $A_y(t)$ and $A_x(t)$ are the time-varying amplitudes of the baseband signals, respectively. Band-pass filtering is implemented by first applying a low-pass filter (LPF) at a maximum Doppler frequency $\omega_{d\,\max} < \omega_m$ [rad/s], after which the DC component and low-frequent oscillations are removed by applying a high-pass filter (HPF) with cut-off $\omega_{d\,\min} < \omega_{d\,\max}$ [rad/s]. This high-pass filter thus sets the lower limit for the speed of motion that can be measured. Second, $v_y(t)$ and $v_x(t)$ have to be normalized to be able to accurately track $\phi_d(t)$. The demodulated Doppler signals are normalized by using the Hilbert transform, as indicated by $H\{\cdot\}$. As the ideal Hilbert transform equals $+j$ for negative frequencies and $-j$ for positive frequencies,[37] it follows that:

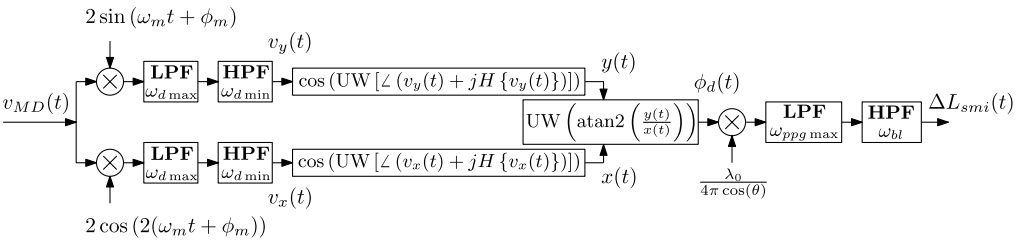

Fig. 3 Block diagram describing how displacement is determined from the monitor diode signal $v_{\mathrm{MD}}(t)$. $H\{\cdot\}$ indicates the Hilbert transform, UW indicates phase unwrapping, and atan2$(\cdot)$ indicates the implementation of the arctangent that takes into account in which quadrant $y(t)$ and $x(t)$ are located.

$$v_y(t)+jH[v_y(t)]=A_y(t)e^{-j\pi/2}e^{j\phi_d(t)}, \tag{13}$$

$$v_x(t)+jH[v_x(t)]=A_x(t)e^{j\phi_d(t)}. \tag{14}$$

By substituting the phase of these analytical signals in a cosine, the normalized baseband signals $y(t)$ [-] and $x(t)$ [-] are obtained:

$$y(t)=\cos[\mathrm{unwrap}(\angle\{v_y(t)+jH[v_y(t)]\})]=\sin[\phi_d(t)], \tag{15}$$

$$x(t)=\cos[\mathrm{unwrap}(\angle\{v_x(t)+jH[v_x(t)]\})]=\cos[\phi_d(t)], \tag{16}$$

in which unwrap removes the discontinuities in the radian phase by adding multiples of $\pm 2\pi$, and $\angle$ indicates the angle of a complex number. Displacement of the laser diode can now be reconstructed by tracking the phase $\phi_d(t)$ [Eq. (7)], which can be obtained by unwrapping the arctangent of the ratio of $y(t)$ and $x(t)$. Considering the one-dimensional motion in the *in vitro* setup, displacement can be determined from phase $\phi_d(t)$ by equating each phase change of 2π rad to a displacement of half a wavelength $\lambda_0/2$, and correcting for the angle θ between the laser beam and the direction of motion:

$$\Delta L_{\mathrm{smi}}(t)=\mathrm{BPF}\left\{\frac{\lambda_0}{4\pi\cos(\theta)}\mathrm{unwrap}\left[\mathrm{atan2}\left(\frac{y(t)}{x(t)}\right)\right]\right\} \tag{17}$$

$$=\mathrm{BPF}\left[\frac{L_o}{\cos(\theta)}\left(1-\frac{\Delta\lambda_{\mathrm{fb}}(t)}{\lambda_0}\right)+\int_0^t v_o(\xi)\mathrm{d}\xi\right], \tag{18}$$

in which atan2$(\cdot)$ refers to an implementation of the arctangent that takes into account in which quadrant $y(t)$ and $x(t)$ are located. The BPF is implemented by an LPF and an HPF (Fig. 3). An LPF with a cut-off at the bandwidth of the PPG, $\omega_{\mathrm{ppg\ max}}$ [rad/s], first makes sure that the motion artifact reference has the same bandwidth as the PPG, in order to avoid introducing additional noise to the PPG. In a practical implementation the HPF with a cut-off at ω_{bl} [rad/s] subsequently removes any baseline drift, with ω_{bl} sufficiently small to accommodate the lowest expected PR.

2.1.3 *Accuracy analysis*

In practice, the demodulated Doppler signals $v_y(t)$ and $v_x(t)$ [Eqs. (11) and (12)] are perturbed by additive noise terms, caused by shot noise, thermal noise, and quantization noise. The influence of these noise terms on the accuracy of the displacement measurement method is investigated in this section. The presence of noise in $v_y(t)$ and $v_x(t)$ can be expressed as:

$$v_{yn}(t)=A_y(t)\sin[\phi_d(t)]+\sum_i A_{yni}(t)\cos[\phi_{yni}(t)], \tag{19}$$

$$v_{xn}(t)=A_x(t)\cos[\phi_d(t)]+\sum_i A_{xni}(t)\cos[\phi_{xni}(t)], \tag{20}$$

in which $A_{yni}(t)$ and $A_{xni}(t)$ are the amplitudes of the noise terms in $v_{yn}(t)$ and $v_{xn}(t)$, respectively, and $\phi_{yni}(t)$ and $\phi_{xni}(t)$ are the phases of the noise terms in $v_{yn}(t)$ and $v_{xn}(t)$, respectively. When assuming an SNR >1, the first order Taylor approximation of the normalized demodulated Doppler signals is:

$$\begin{aligned}y_n(t)&=\cos[\mathrm{unwrap}(\angle\{v_{yn}(t)+jH[v_{yn}(t)]\})]\\&\approx\sin\left[\phi_d(t)+\frac{3}{2}\sum_i\frac{A_{yni}(t)}{A_y(t)}\right],\end{aligned} \tag{21}$$

$$\begin{aligned}x_n(t)&=\cos[\mathrm{unwrap}(\angle\{v_{xn}(t)+jH[v_{xn}(t)]\})]\\&\approx\cos\left[\phi_d(t)+\frac{3}{2}\sum_i\frac{A_{xni}(t)}{A_x(t)}\right].\end{aligned} \tag{22}$$

By using Eqs. (21) and (22) for $y(t)$ and $x(t)$ in Eq. (17), and once more assuming an SNR >1, the following first order Taylor approximation is obtained for the displacement (omitting the BPF for brevity):

$$\begin{aligned}\Delta L_{\mathrm{smi}n}(t)=&\frac{\lambda_0}{4\pi\cos(\theta)}\\&\times\mathrm{unwrap}\left(\mathrm{atan2}\left\{\frac{\sin\left[\phi_d(t)+\frac{3}{2}\sum_i\frac{A_{yni}(t)}{A_y(t)}\right]}{\cos\left[\phi_d(t)+\frac{3}{2}\sum_i\frac{A_{xni}(t)}{A_x(t)}\right]}\right\}\right)\end{aligned} \tag{23}$$

$$\begin{aligned}&\approx\frac{L_o}{\cos(\theta)}+\int_0^t v_o(\xi)\mathrm{d}\xi-\frac{L_o}{\lambda_0}\frac{\Delta\lambda_{fb}(t)}{\cos(\theta)}+\frac{\frac{3}{2}\frac{\lambda_0}{4\pi\cos(\theta)}}{1+\tan^2[\phi_d(t)]}\\&\cdot\left\{\sum_i\frac{A_{yni}(t)}{A_y(t)}+\tan^2[\phi_d(t)]\sum_i\frac{A_{xni}(t)}{A_x(t)}\right\}\end{aligned} \tag{24}$$

$$\leq \frac{L_o}{\cos(\theta)} + \int_0^t v_o(\xi)\mathrm{d}\xi + \frac{\lambda_0}{4\pi\,\cos(\theta)} C + \frac{\frac{3}{2}\lambda_0}{4\pi\,\cos(\theta)} \cdot \max_t \left[\sum_i \frac{A_{yni}(t)}{A_y(t)} + \sum_i \frac{A_{xni}(t)}{A_x(t)} \right], \quad (25)$$

in which the change in wavelength as a result of optical feedback, $\Delta\lambda_{\mathrm{fb}}(t)$, has been replaced by an upper bound using the lasing condition and optical feedback parameter C [-].[30] Equation (25) shows the upper bound of two additive noise sources which distort the displacement measurement, for SNR > 1. The first noise source is caused by the change in emitted optical wavelength as a result of optical feedback and has been replaced by upper bound $(\lambda_0 C)/[4\pi\,\cos(\theta)]$. Because only (very) weak feedback regimes are expected in this application, it holds that the feedback parameter $C < 1$.[30] Therefore, this error term will have a magnitude on the order of $(\lambda_0 C)/[4\pi\cos(\theta)] \sim 10^{-8} - 10^{-7}$ m. The second noise source, being a result of shot noise, thermal noise, and quantization noise, is inversely proportional to the SNR of the Doppler signals. For SNR > 1, also this term has a magnitude of $10^{-8} - 10^{-7}$ m. Because sensor displacement is expected to be on the order of $10^{-4} - 10^{-3}$ m, these error sources introduce a negligibly small error of roughly 0.1‰–1‰, as long as the SNR > 1. However, speckle can cause the amplitude of the Doppler signals to become very small, resulting in an SNR < 1, in which case the contribution of the second noise source cannot be neglected anymore. Destructive speckle interference may occur when the surface roughness of the illuminated object is such that the backscattered contributions of the laser light cancel at the laser. This phenomenon cannot be prevented. Therefore, destructive speckle interference is expected to be the dominant cause of inaccuracies in the displacement measurement, but the exact impact depends on the illuminated surface.

Inaccuracies also result because the average emission wavelength λ_0 and the angle θ between the laser beam and the direction of motion are not exactly known. The emission wavelength of the 850 nm VCSEL is specified with an accuracy of 10 nm, which thus may result in a displacement error of approximately 1%.[38] Fluctuations in the emission wavelength as a result of modulation and optical feedback are negligible. Modulation of the injection current results in minor wavelength variations on the order of 10^{-12} m (see Sec. 2.1.1). Moreover, from Eqs. (24) and (25) it follows that optical feedback only changes the wavelength by at most $(\lambda_0^2 C)/(4\pi L_o) \sim 10^{-12}$ m. The inaccuracy $\delta\theta$ in the angle θ results in a displacement error of $[\tan(\theta)/\cos(\theta)]\delta\theta \approx 3.5 \cdot \delta\theta$ for $\theta = \pi/3$ rad, which equals approximately 6% for $\delta\theta = \pi/180$ rad. The effect of the inaccuracy in angle θ thus dominates the effect of wavelength inaccuracy. However, these inaccuracies are both constant scaling effects on the amplitude of the displacement measurement. Exactly measuring the absolute displacement is not relevant in the context of PPG motion artifact reduction. In this context, it is most important to accurately measure the frequency of motion of the sensor.

2.2 *Experimental Setup*

An *in vitro* setup has been built to study whether it is possible to remove motion artifacts from a PPG by using relative sensor motion as an artifact reference. This setup contains a flow cell that mimics skin perfusion, as described in Sec. 2.2.1. Section 2.2.2 describes how this flow cell is used in a setup to obtain motion corrupted PPGs *in vitro*.

2.2.1 *Skin perfusion phantom*

To be able to measure PPGs *in vitro*, a flow cell has been made that models cardiac induced blood volume changes in the skin. Figure 4 shows a cross-sectional view of the flow cell, Fig. 5(a) shows the different components of this flow cell, and Fig. 5(b) shows the assembled flow cell. Two different inserts have been made that go into the base of the flow cell. Both inserts define a rectangular flow channel that is 170 mm long and 34.7 mm wide. In both inserts, half of the flow channel is 0.5 mm deep and half is 1 mm deep, with an abrupt change in depth in the middle. In this study, PPGs have only been measured over the 1 mm deep channel. One insert defines a rigid flow channel, and the other insert contains two 29.7 mm by 45.8 mm silicone membranes to realize a flexible flow channel [Fig. 5(a)]. Below the membranes, this insert contains air filled chambers, which are connected to ambient air via a channel in the base. Either a transparent or a Delrin® (polyoxymethylene, POM) window of 1 mm high is mounted on top of the base and the insert to close off the flow channel. The window is fixed via a stainless steel ring, as shown in Fig. 5(b).

Because the pulsatility in the PPG originates from the dermis, the flow channel has been closed off by a 1 mm high POM skin phantom.[39–41] A diffuse scattering POM window has been used as a skin phantom, because the optical properties of POM are similar to skin.[42] The POM window models the optical shunt caused by light that does not propagate through pulsating blood, as illustrated by the topmost dashed arrow in Fig. 4.[2,41] A transparent window has been used to determine the contribution of the optical shunt through the POM skin phantom to the modeled PPG.

Because the topmost layers of the skin contain a dense network of capillaries and microvessels, blood flow has been

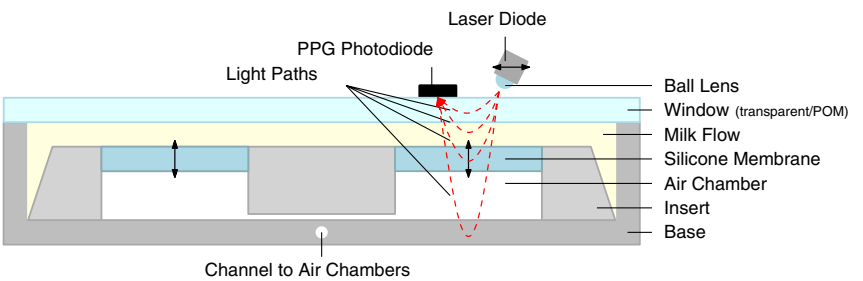

Fig. 4 Cross-sectional view of the flow cell containing the insert with silicone membranes (not to scale). The dashed arrows indicate different light paths that contribute to the PPG photodiode signal. The solid arrows indicate motion of the membranes to mimic changing blood volume and motion of the laser diode to generate artifacts.

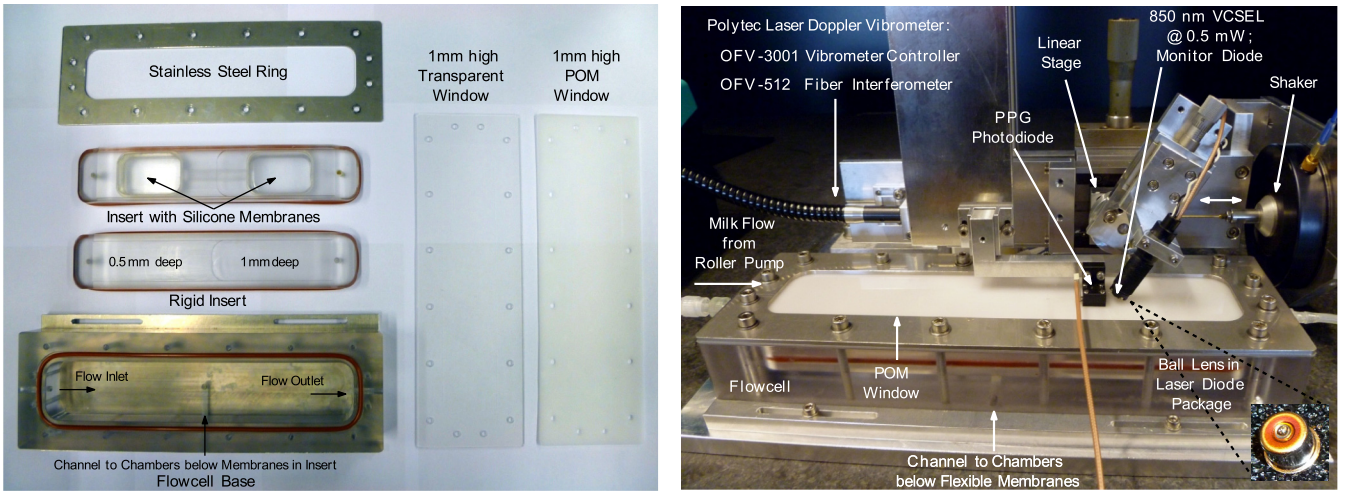

Fig. 5 (a) The components of the flow cell that has been developed as a skin perfusion phantom. The inserts go into the base of the flow cell and define the flow channel. The top of the flow channel is closed off by either a transparent or a POM window. (b) The assembled flow cell in the experimental setup built to measure PPGs distorted by optical motion artifacts. Optical motion artifacts are generated by translating the laser diode with respect to the PPG photodiode.

modeled by a thin layer of flow.[40,41] By using the insert with the silicone membranes, a flexible flow channel is obtained that enables mimicking blood volume changes. A pulsatile flow will cause the flexible membranes to bend downward upon increases in pressure in the channel, thus locally increasing the volume of the flow channel, as indicated in Fig. 4. The insert with the rigid flow channel has been used to verify that the volume increase indeed is the origin of the pulse in the modeled PPG.

Finally, milk has been used to mimic blood, because both milk and blood contain light scattering particles which are comparable in size.[43] In blood, erythrocytes scatter light, which have a typical diameter of 8 μm.[44] In milk, fat globules scatter light, which have a diameter between 1 μm and 10 μm with an average of 4 μm.[45] Furthermore, it is known that also in reflective measurements the PPG mainly results from increases in light attenuation; any increase in directly backscattered light as a result of increased blood volume is usually negligible compared to the increased absorption of light returning from deeper tissue, for source-detector distances of approximately 1 cm.[10,46] Therefore, because milk hardly absorbs at 850 nm, a small amount of a water-soluble black dye has been added as an absorber.[47]

2.2.2 *Measurement setup*

The setup in Fig. 5(b) is used to measure PPGs and generate optical motion artifacts. An 850 nm vertical-cavity surface-emitting laser diode (VCSEL) with an internal monitor diode is used to illuminate the flow cell. A roller pump with three rollers generates a pulsatile milk flow, which results in a varying milk volume in the flow cell. The photodiode on top of the flow cell's window [PPG Photodiode in Figs. 4 and 5(b)] measures a PPG when the laser diode illuminates the flow cell. The distance between the laser spot on the flow cell's window and the center of the photodiode is approximately 1 cm. The laser diode is attached to a linear stage, which is driven by a shaker. In this way, the shaker can translate the laser diode to generate motion artifacts in the PPG as a result of a dynamically changing emitter-detector distance. Artifacts result because the change in emitter-detector distance alters the optical shunt through the POM window and changes the depth at which the light probes the perfusion phantom (Fig. 4).[41] In practice, these effects result from sensor deformation or when the whole PPG sensor translates over inhomogeneous tissue.

Sufficiently strong optical feedback is required to measure displacement of the laser diode using SMI. Therefore, the laser beam is focused on the flow cell's window via the ball lens that has been integrated in the laser diode package. A close-up of the laser diode package with integrated ball lens is shown bottom right in Fig. 5(b). This compact component has been used to be able to readily integrate it in a real sensor later on. The distance between the ball lens and the window is approximately 2 mm, resulting in a distance $L_o \approx 4$ mm between the laser diode and the window. The angle between the laser beam and the flow cell's surface normal is 30-deg. To verify the SMI displacement measurement, a reference displacement measurement is obtained by a laser Doppler vibrometer (LDV) (Polytec, Waldbronn, Germany). Here the OFV-3001 Vibrometer Controller has been used combined with the OFV-512 Fiber Interferometer. The LDV directly measures the translation of the linear stage [Fig. 5(b)]. By limiting the displacement of the linear stage to 1280 μm, the LDV has a resolution of 0.32 μm.

A laser driver controls the injection current of the laser diode. An optical output power of 0.5 mW is obtained at a DC current of 1.63 mA. The DC level of the laser's monitor diode is visually inspected to confirm that the laser's optical output power does not change during the measurements. A 40-kHz AC current with an amplitude of 158 μA is superimposed to obtain the desired ϕ_0 that minimizes the Doppler signals in the baseband, as described in Sec. 2.1.1. The laser driver generates the 40-kHz AC current from a 40-kHz AC voltage that is provided by a function generator (33250A 80 MHz Function/Arbitrary Waveform Generator, Agilent Technologies, Inc., Santa Clara, California). For the 850 nm VCSEL that is used, the lasing wavelength dependency on the injection current is specified to be 0.4 nm/mA.[38] The modulation induced wavelength change thus is approximately 63 pm, resulting in $\Delta\lambda_m/\lambda_0 \approx 7 \cdot 10^{-5}$, which is comparable

to the required wavelength modulation stated at the end of Sec. 2.1.1, given the inaccuracies and temperature dependencies of the laser diode parameters.

The PPG photodiode and monitor diode currents are amplified by transimpedance amplifiers to obtain the voltages $v_{\mathrm{PD}}(t)$ and $v_{\mathrm{MD}}(t)$, respectively. The PPG photodiode and monitor diode voltages, and the LDV signal are band limited at 100 kHz and recorded at 200 kHz by a 16 bit digital data acquisition card (DAQ) (NI USB-6259, National Instruments, Austin, Texas). A LabVIEW® (National Instruments, Austin, Texas) program controls the DAQ. The LabVIEW® program also generates the signal that is sent out by the DAQ and amplified to control the shaker. PPGs are obtained by band limiting $v_{\mathrm{PD}}(t)$ at 30 Hz. Finally, a 10-MHz input clock-signal for the function generator is derived from the DAQ's 20-MHz clock signal, to make sure that only one clock is used in the measurement system.

2.3 *PPG Motion Artifact Reduction*

An NLMS algorithm reduces the optical motion artifacts in the corrupted PPG by using the laser's displacement as an artifact reference. To obtain insight in the performance of the NLMS algorithm, the distorted PPG is first coarsely modeled using the Beer-Lambert law to determine how it is affected by changes in channel volume and emitter-detector distance.

2.3.1 *Modeling the PPG*

Figure 4 illustrates the contribution of different light paths to the signal that is detected by the PPG photodiode. As indicated from top to bottom by the four dashed arrows in Fig. 4, laser light that reaches the PPG photodiode has either propagated through the window directly, through the window and the milk, through the window, the milk and the membrane, or it has been backscattered by the base of the flow cell. The detected light intensity can be modeled coarsely by making use of the Beer-Lambert law, which is commonly employed in pulse oximetry:[2,3,46]

$$\begin{aligned} P_d(t) \approx P_0(&\exp\{-\alpha_w l_w[L_{\mathrm{ed}}(t)]\} \\ &+ \exp\{-2\alpha_w l_{wm} - \alpha_m l_m[L_{\mathrm{ed}}(t), V_m(t)]\} \\ &+ \exp\{-2\alpha_w l_{wm} - 2\alpha_m l_{ms}[L_{\mathrm{ed}}(t), V_m(t)] \\ &- \alpha_s l_s[L_{\mathrm{ed}}(t), V_m(t)]\} \\ &+ \exp\{-2\alpha_w l_{wm} - 2\alpha_m l_{ms}[L_{\mathrm{ed}}(t), V_m(t)] \\ &- 2\alpha_s l_{sb}[L_{\mathrm{ed}}(t), V_m(t)] - \alpha_b l_b[L_{\mathrm{ed}}(t)]\}), \end{aligned} \tag{26}$$

in which P_0 [W] and $P_d(t)$ [W] are the emitted and detected light power, respectively, $\alpha\,[\mathrm{m}^{-1}]$ is the extinction coefficient, l [m] is the optical path length, $L_{\mathrm{ed}}(t)$ [m] is the emitter-detector distance, $V_m(t)$ [m^3] is the milk volume in the channel, and subscripts w, wm, m, ms, s, sb, and b, stand for window, from window to milk, milk, from milk to silicone, silicone, from silicone to base, and base, respectively. The first exponent in Eq. (26) describes the optical shunt through the window. The optical path through the window is a function of emitter-detector distance. The second exponent describes light that has propagated through the window and the milk. The factor two in the first term of the exponent indicates that the light has traveled through the window twice. The optical path length through the milk is a function of emitter-detector distance and milk volume in the channel. Both an increase in emitter-detector distance and an increase in milk volume extend the path through the milk. The third exponent describes light that has traveled back to the photodiode via the silicone membrane. In this component, the optical paths via the milk to the silicone and in the silicone are a function of emitter-detector distance and milk volume. An increase in milk volume will increase the optical path through the milk, but emitter-detector distance will only influence the path via the milk to the membrane when an increased milk volume causes the channel height to be nonuniform. The path length through the silicone is a function of emitter-detector distance, because this distance influences the path length that photons have to travel through the membrane to be able to reach the photodiode. Because the membrane's shape depends on milk volume, the path through the silicone is a function of milk volume too. The fourth exponent describes light that has been backscattered by the base of the flow cell. The third term in this exponent describes light propagating through the silicone. This light path depends on milk volume, because an increase in milk volume deforms the silicone. Furthermore, the path through the silicone depends on emitter-detector distance only if the membrane has been deformed by the milk volume such that it has a nonuniform thickness. The last term in this exponent describes the optical path that the light travels through the base of the flow cell before it is backscattered towards the photodiode. The distance that detected photons have traveled through the base also depends on the emitter-detector distance.

To obtain more insight in the direct relationship between laser motion and the detected optical signal, one can determine a Taylor approximation of Eq. (26). The approximation around the stationary condition in which both milk volume and emitter-detector distance are constant, equals:

$$P_d(t) \approx P_0[c_0 - c_1\Delta V_m(t) - c_2\Delta L_{ed}(t) - c_3\Delta L_{ed}(t)\Delta V_m(t)], \tag{27}$$

in which c_0 [-], c_1 [m^{-3}], c_2 [m^{-1}] and c_3 [m^{-4}] are proportionality constants, $\Delta V_m(t)$ [m^3] is a small time-varying variation in milk volume in the channel, and $\Delta L_{\mathrm{ed}}(t)$ [m] is a small time-varying deviation of the emitter-detector distance caused by the shaker action. This approximation shows that the laser's motion mainly distorts the PPG, $-c_1\Delta V_m(t)P_0$, by an additive artifact $-c_2\Delta L_{\mathrm{ed}}(t)P_0$ directly proportional to the variation in emitter-detector distance, and by a multiplicative artifact $-c_3\Delta L_{\mathrm{ed}}(t)\Delta V_m(t)P_0$.

2.3.2 *NLMS algorithm*

Based on the Taylor approximation in Eq. (27), which describes the influence of laser motion on the PPG, an NLMS algorithm[29] is used in a first attempt to reduce the motion artifacts in the PPG. If the NLMS algorithm succeeds in reducing the motion artifacts by using the laser displacement as an artifact reference, this also proves correlation between the displacement measurement and the artifacts.

The implemented NLMS algorithm, as illustrated in Fig. 6, subtracts the reconstructed motion artifact $h_0[k]\Delta l_{\mathrm{ma}}[k]$ from the zero-mean photodiode signal $\tilde{\mathrm{v}}_{\mathrm{PD}}[k]$ in order to recover $\mathrm{ppg}[k]$, i.e., the PPG. Here k is a discrete time index, $h_0[k]$ is the adaptive filter coefficient, and $\Delta l_{\mathrm{ma}}[k]$ is the laser displacement scaled by its RMS value. The RMS value is determined over the entire length of the recording. The same 0.3-Hz HPF that is applied to the SMI displacement measurement (Fig. 3) is used to remove

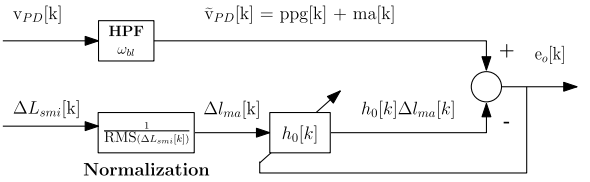

Fig. 6 NLMS structure that removes motion artifact ma[k] that distorts ppg[k], i.e., the PPG, in the zero-mean photodiode signal $\tilde{v}_{\mathrm{PD}}[k]$. The motion artifact is reconstructed using the zero-mean laser displacement $\Delta L_{\mathrm{smi}}[k]$ and a filter with one coefficient $h_0[k]$. The displacement is normalized by its RMS value to obtain $\Delta l_{\mathrm{ma}}[k]$.

the mean from the photodiode signal. All inputs to the NLMS algorithm have been downsampled to 250 Hz. The optimal FIR filter h_0 for motion artifact reconstruction is determined by iteratively minimizing the power of output signal $e_o[k]$:[29]

$$\min_{h_0} e_o^2[k] = \min_{h_0} [\tilde{\mathrm{v}}_{\mathrm{PD}}(k) - h_0(k)\Delta l_{\mathrm{ma}}(k)]^2, \tag{28}$$

$$\begin{aligned} h_0(k+1) &= h_0(k) - \mu \nabla_{h_0} e_o^2(k) \\ &= h_0(k) + 2\mu e_o(k)\Delta l_{\mathrm{ma}}(k), \end{aligned} \tag{29}$$

$$\Delta l_{\mathrm{ma}}[k] = \frac{\Delta L_{\mathrm{smi}}[k]}{\sqrt{\frac{1}{N_{\mathrm{rec}}}\sum_{l=1}^{N_{\mathrm{rec}}} \Delta L_{\mathrm{smi}}^2[l]}}, \tag{30}$$

with step-size parameter μ and recording length N_{rec} [samples]. The minimum of the output power is determined by successively taking steps in the opposite direction of its gradient, $\nabla_{h_0} e_o^2[k]$, with step-size μ. When $h_0[k]$ has converged, the minimum output power has been found and $e_o[k]$ does not contain any information anymore that correlates with $\Delta l_{\mathrm{ma}}[k]$. Ideally, only the PPG remains after convergence, which would imply high correlation between $\Delta l_{\mathrm{ma}}[k]$ and the motion artifacts, and no correlation between $\Delta l_{\mathrm{ma}}[k]$ and the PPG. The artifact reduction achieved by the NLMS algorithm is quantified by:

$$Q = 10 \cdot \log\left\{ \frac{\sum_{k=1}^{N_{\mathrm{rec}}} [e_o(k) - \mathrm{ppg}_{\mathrm{ref}}(k)]^2}{\sum_{k=1}^{N_{\mathrm{rec}}} [\tilde{\mathrm{v}}_{\mathrm{PD}}(k) - \mathrm{ppg}_{\mathrm{ref}}(k)]^2} \right\}, \tag{31}$$

in which $\mathrm{ppg}_{\mathrm{ref}}[k]$ is the reference PPG measured in the flow cell when the laser diode is stationary.

3 Experimental Results

3.1 *Measuring Displacement*

When the laser beam is focussed on the POM window, the laser's displacement can be measured using SMI, by processing the monitor diode signal as outlined in Fig. 3. In this section, the measured Doppler signals, the effects of speckle and the accuracy of the displacement measurement are discussed.

3.1.1 *Doppler signals*

Figure 7 shows the spectrogram of the monitor diode signal when the shaker is driven by a 2-Hz sinusoid with an amplitude such that the peak-to-peak displacement is approximately 1 mm. Doppler signals as a result of laser motion can be observed in the baseband, around the modulation frequency at 40 kHz, and its second harmonic at 80 kHz. In each of these three frequency bands, weak second harmonics of the Doppler frequencies themselves can be observed, indicating weak optical feedback and an interference pattern which is not perfectly sinusoidal.[32,33] Furthermore, the spectrogram shows that the used modulation depth of the laser injection current effectively reduces the magnitude of the Doppler signals in the baseband, and results in Doppler signals of comparable magnitude in the frequency bands around 40 and 80 kHz, as explained by Eqs. (8) and (10).

Demodulation of the monitor diode signal as described by Eqs. (11) and (12) yields the baseband Doppler signals $v_y(t)$ and $v_x(t)$ as shown by the dashed and solid curves in Fig. 8, respectively. The carriers required for demodulation are reconstructed in MATLAB (MathWorks, Natick, Massachusetts), by determining the phase ϕ_m that yields maximum correlation between a 40-kHz sine and the monitor diode signal. The resulting phase ϕ_m is subsequently used to construct a locked 80-kHz cosine [Eq. (10)]. Finally, a 15-kHz LPF and a 10-Hz HPF are applied to bandlimit the demodulated Doppler signals ($\omega_{d\,\max}$ and $\omega_{d\,\min}$ in Fig. 3, respectively). Therefore, from Eq. (1) it follows that this system can track velocities between 8.5 μm/s and 12.75 mm/s, which is expected to be sufficient for the intended application. The segment in Fig. 8 shows a change in the laser's direction of motion: at first the Doppler frequency decreases, and when it starts increasing again, the order of the signals' local extremes has changed, which indicates the change in direction. The normalized Doppler signals $y(t)$ and $x(t)$ as obtained via the Hilbert transform [Eqs. (15) and (16)] are shown by the dashed and solid curves in Fig. 9, respectively (this is a different segment than shown in Fig. 8). Overall, effective normalization is obtained via the Hilbert transform.

3.1.2 *Speckle effects*

Speckles cause a strong variation of the amplitude of the Doppler signals, as illustrated in Fig. 8: here the local minima result from destructive speckle interference. Furthermore, when destructive speckle interference strongly reduces the amplitude of the Doppler signals, proper normalization is no longer possible; this occurs during the moments indicated by arrows 1 and 2 in Fig. 9. In addition, speckle interference can cause jumps of π rad in the phase of the Doppler signals, as indicated by arrows 3 and 4 in Fig. 9.

To quantify the effect of speckle on the SNR of the Doppler signals, a conservative estimate of the SNR of the baseband Doppler signals has been determined as follows. The magnitude

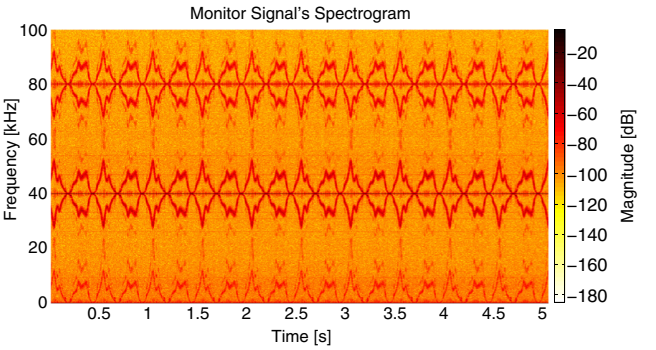

Fig. 7 Spectrogram of monitor signal $v_{\mathrm{MD}}(t)$. Doppler signals as a result of laser motion can be observed in the baseband, around the modulation frequency at 40 kHz, and around the second harmonic at 80 kHz.

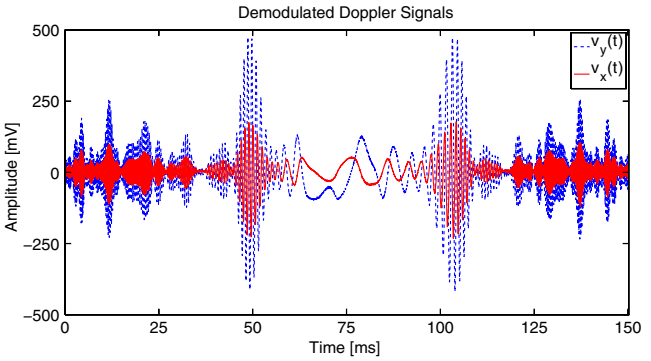

Fig. 8 Segment of the baseband Doppler signals $v_y(t)$ and $v_x(t)$ obtained by demodulating monitor signal $v_{MD}(t)$. The strong variation of the signals' amplitude is caused by speckle effects.

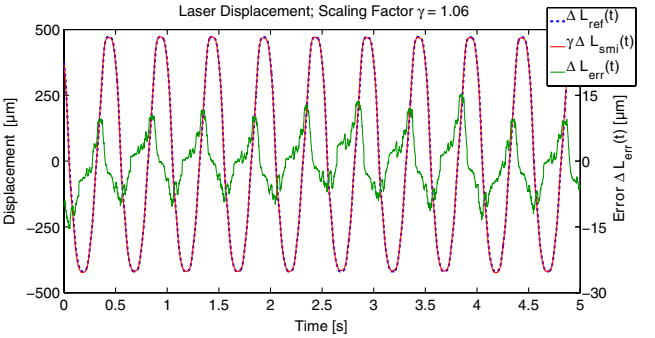

Fig. 10 The laser displacement measured via SMI and scaled by $\gamma = 1.06$ (heavy solid curve), the reference LDV measurement (heavy dashed curve), and their difference $\Delta L_{err}(t) = \gamma \Delta L_{smi}(t) - \Delta L_{ref}(t)$ (thin curve). The difference has been shown explicitly, because the SMI and LDV displacement measurements are almost identical.

of the Hilbert transform of the baseband Doppler signals $v_{yn}(t)$ and $v_{xn}(t)$ is used to determine the instantaneous amplitude of the signals containing noise, $S_y(t)$ and $S_x(t)$, respectively. Background noise signals $n_y(t)$ and $n_x(t)$ in the signal bands around 40 kHz and 80 kHz, respectively, have been determined by applying the demodulation scheme in Fig. 3 to the monitor diode signal that was measured when the laser diode did not experience any optical feedback. This condition was obtained by placing black foam approximately 4 cm in front of the ball lens. The conservative SNR estimates have been obtained by dividing the signal strengths by three times the RMS value of the background noise, i.e., $\mathrm{SNR}_y = S_y(t)/\{3 \cdot \mathrm{RMS}[n_y(t)]\}$ and $\mathrm{SNR}_x = S_x(t)/\{3 \cdot \mathrm{RMS}[n_x(t)]\}$. Both baseband Doppler signals have comparable SNRs: $\mathrm{SNR}_y = 23.9$ dB on average in a range from -53.6 dB to 38.2 dB, and $\mathrm{SNR}_x = 23.0$ dB on average in a range from -45.6 dB to 38.3 dB. SNR < 1 of either of the baseband Doppler signals occurs only during approximately 1% of the recording.

3.1.3 *Accuracy*

The heavy solid curve in Fig. 10 shows the displacement $\Delta L_{smi}(t)$ obtained via Eq. (17) with $\theta = 60$-deg., and scaled by $\gamma = 1.06$. As described in Sec. 2.1.3, the displacement measured via SMI can contain a constant scaling error. This scaling error has been accounted for by the factor γ [-]. The scaling error has been estimated by determining the scaling factor γ that minimizes the mean squared error between $\gamma \Delta L_{smi}(t)$ and $\Delta L_{ref}(t)$. This error is minimized by taking the value $\gamma = 1.06$. Furthermore, Fig. 10 shows the LDV reference $\Delta L_{ref}(t)$ (dashed curve), and the difference $\Delta L_{err}(t) = \gamma \Delta L_{smi}(t) - \Delta L_{ref}(t)$ (thin solid curve). The difference has been shown explicitly, because the SMI and LDV displacement measurements are almost identical. Baseline drift is removed from the displacement measurement by applying a 0.3-Hz HPF (ω_{bl} in Fig. 3). The remaining error $\Delta L_{err}(t)$ equals 0.09 ± 6 μm (mean $\pm$ RMS).

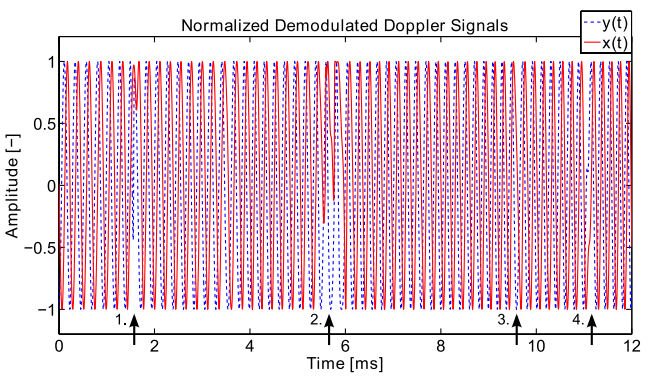

Fig. 9 Segment of the normalized baseband Doppler signals $y(t)$ and $x(t)$. Arrows 1 and 2 indicate moments during which normalization is not effective, because destructive speckle interference strongly decreases the amplitude of the original Doppler signals. Arrows 3 and 4 indicate moments at which a jump of π rad occurs in the phase of the Doppler signals, which is also caused by speckle interference. This is a different segment than shown in Fig. 8.

3.2 *Measuring In Vitro PPGs*

In vitro PPGs have been measured in three different ways: by using milk in the insert with the rigid channel (case 1), by using milk in the insert with the silicone membranes (case 2), and by using milk with a water-soluble black dye in the insert with the silicone membranes (case 3). In all cases the roller-pump was used at 20 RPM to generate a pulsatile flow, thus simulating a pulse rate of 60 BPM. Cases 1 and 2 were used to verify that the change in milk volume in the flexible channel represents the dominant contribution to the PPG amplitude. The measured PPGs are shown by the solid curves in Fig. 11. Furthermore, via SMI the deflection of the POM window was measured, as shown by the dashed curves in Fig. 11. Here, the angle θ between the laser beam and the direction of motion equals 30-deg., and an offset has been added to the displacement such that its minimum is 0 μm.

In case 1, a PPG is measured with a 5.5 mV peak-to-peak amplitude, and the POM window moves upward by approximately 55 μm [Fig. 11(a)]. In case 2, a PPG is measured with a 13 mV peak-to-peak amplitude, the DC level increases by approximately 100 mV compared to case 1, and the window moves upward by only 23 μm [Fig. 11(b)]. Moreover, in cases 1 and 2 the PPG is in phase with the window deflection. In case 3 however, the PPG is in antiphase with the window deflection [Fig. 11(c)]. The increased absorption has furthermore lowered the PPG amplitude to 11 mV and its DC level to 268 mV. In case 3, the PPG's amplitude equals approximately 4% of its DC level.

Measurements have also been done using a transparent window, to determine the influence of POM. Compared to the transparent window, the POM window causes a decrease in the PPG's DC level and amplitude. The decrease in amplitude is a

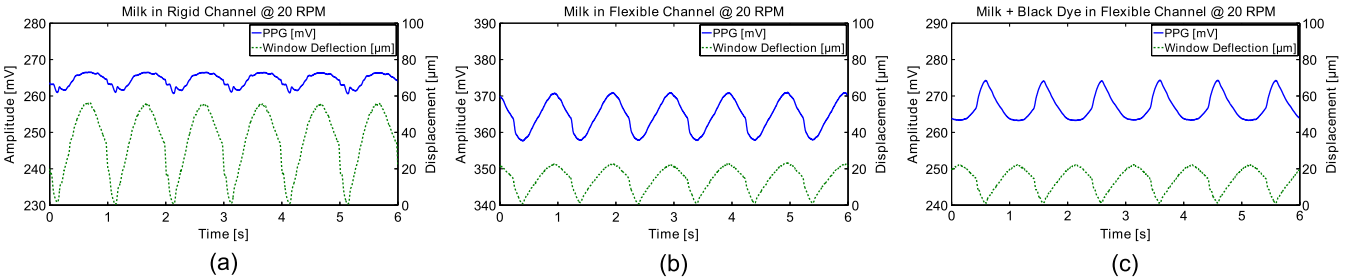

Fig. 11 PPGs measured in the flow cell (solid curves) with the roller pump set at 20 RPM. The deflection of the POM window (dashed curves) is measured via SMI with $\theta = 30$-deg. (a) Milk flows through the rigid channel. (b) Milk flows through the channel with the silicone membranes. (c) Milk with a water-soluble black dye flows through the channel with the silicone membranes.

result of additional attenuation [Eq. (26)]. Moreover, in combination with milk, the POM window introduces an optical shunt, because the PPG's amplitude decreases by a larger factor than its DC level does [Eq. (26)].

3.3 *Motion Artifact Reduction*

Figure 12 illustrates the reduction of optical motion artifacts using NLMS with the SMI displacement measurement as an artifact reference (Fig. 6). Artifacts as a result of laser motion have been generated by steering the shaker with a 0.5 to 10 Hz band-pass filtered white noise sequence. All PPGs have been measured using milk containing a water-soluble black dye, the insert with the silicone membranes, and a POM window. All inputs to the NLMS algorithm have zero mean. Zero-mean PPGs have been obtained by applying the same 0.3-Hz HPF as is applied to the SMI displacement measurement (ω_{bl} in Fig. 3). The NLMS algorithm has been trained using step-size parameter $\mu = 0.01$ and filter order $N_f = 1$. Because displacement of the laser diode is measured directly, no mechanical transfer function is expected between the laser displacement and the resulting optical effect. Displacement of the laser diode furthermore directly affects the optical path through the flow cell, no hysteresis and memory effects are expected. Therefore, a good estimate of the optical artifacts is obtained by adaptively scaling the laser displacement by a single filter coefficient.

First, the reduction of pure optical motion artifacts is considered. Pure artifacts are obtained by translating the laser diode, but keeping the milk volume in the channel constant (roller pump switched off). The reduction of a pure artifact is illustrated by

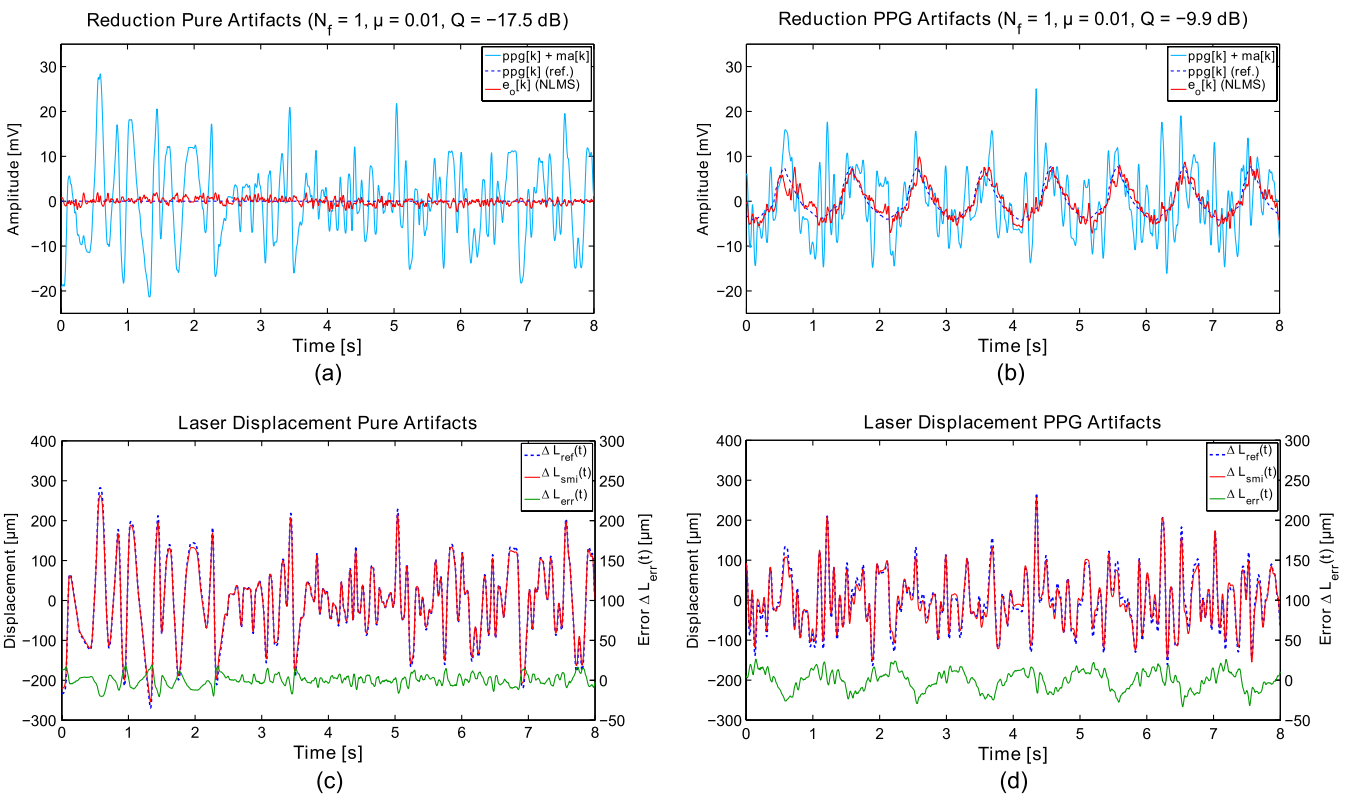

Fig. 12 (a) Reduction of pure motion artifacts. (b) Reduction of motion artifacts corrupting a PPG. In (a) and (b), the thin curve shows the motion corrupted signal, the heavy solid curve shows the NLMS output, and the heavy dashed curve shows the reference signal. (c) Laser displacement causing the pure artifacts in (a). (d) Laser displacement causing the motion artifacts in (b). In (c) and (d), the heavy solid and dashed curves show the displacement measured via SMI and the LDV, respectively, and the thin curve shows their difference $\Delta L_{err}(t) = \Delta L_{smi}(t) - \Delta L_{ref}(t)$. The difference has been shown explicitly, because the SMI and LDV displacement measurements are almost identical.

the three PPGs shown in Fig. 12(a). The thin curve shows the pure optical motion artifact and the heavy curve shows the result of NLMS motion artifact reduction. The dashed curve shows the reference PPG, as measured while the laser diode was stationary, and which is the background noise in the PPG photodiode signal. An artifact reduction of $Q = -17.5$ dB is achieved. Figure 12(c) shows the laser displacement that results in the pure optical motion artifact in Fig. 12(a). The heavy solid and dashed curves in Fig. 12(c) show the SMI and LDV result, respectively; the thin curve is their difference, which has been shown explicitly because the SMI and LDV result are almost identical.

Second, the reduction of an optical motion artifact corrupting a PPG is considered. Corrupted PPGs are obtained by translating the laser diode, while the roller pump generates a pulsatile flow at 20 RPM. The reduction of a motion artifact corrupting a PPG is illustrated by the three PPGs in Fig. 12(b). The thin curve shows the corrupted PPG and the heavy curve shows the result of NLMS motion artifact reduction. The dashed curve shows the reference PPG, as measured by illuminating the pulsating milk volume by a stationary laser. The reference and motion corrupted PPGs have been synchronized by determining the lag at which the maximum correlation between these signals occurs. The artifact reduction has now decreased to $Q = -9.9$ dB. Figure 12(d) shows the laser displacement that causes the corrupted PPG in Fig. 12(b). The heavy solid and dashed curves in Fig. 12(d) show the SMI and LDV result, respectively; the thin curve is their difference, which has been shown explicitly because the SMI and LDV result are almost identical.

Finally, Fig. 13 illustrates the fast convergence of the NLMS algorithm: filter weight $h_0[k]$ (dashed curve) and the output power $e_o^2[k]$ (solid curve) converge within 0.5 s. Furthermore, $h_0[k]$ fluctuates little when reducing pure artifacts [Fig. 13(a)], whereas it fluctuates strongly when reducing artifacts in a corrupted PPG [Fig. 13(b)].

4 Discussion

4.1 *Measuring Displacement*

Comparing the displacement measured via SMI to the LDV reference shows that both displacement measurements are equal in shape (Fig. 10). Moreover, motion towards the LDV gives a positive sign, which confirms that motion towards the laser beam of the VCSEL indeed results in a positive displacement measured via SMI, as indicated by Eqs. (1) and (17).

The precision of the SMI displacement measurement can predominantly be ascribed to speckle interference.[32] As shown in Fig. 8, destructive speckle interference repeatedly causes the Doppler signals' amplitude to fade. As a result of destructive speckle interference, normalization of the Doppler signals is ineffective and interference fringes are missed on a structural basis, as indicated by arrows 1 and 2 in Fig. 9. Furthermore, speckle interference leads to jumps of π rad in the phase of the Doppler signals, as indicated by arrows 3 and 4 in Fig. 9, or other irregularities in the phase of the Doppler signals. These effects of speckle interference lead to structural inaccuracies in the displacement measurement, which results in a baseline drift in the displacement measurement. The slope of the drift depends on the number of speckle interference events per unit of time, and thus on the surface roughness and the speed of motion. Baseline drift occurs in this recording, even though SNR < 1 of either of the baseband Doppler signals occurs only during approximately 1% of the recording time. However, the baseline drift is effectively removed by the 0.3-Hz HPF (ω_{bl} in Fig. 3).

Furthermore, as indicated by γ, the constant scaling error is 6%, which can be explained by an error of approximately 1-deg. in the angle between the laser beam and the direction of motion. However, it is likely that the inaccuracy in the angle θ is smaller than 1-deg., and that γ corrects for the inaccuracy in wavelength λ_0 as well. In addition, it is expected that the effects of speckle interference also lead to a structural error in the amplitude of the displacement measurement, for which γ partly corrects too.

The error in the final displacement measurement is on the order of 10^{-6} m (Fig. 10). A precision of 10^{-6} m is sufficient, since sensor motion is expected to be on the order of $10^{-4} - 10^{-3}$ m. Therefore, this measurement shows that translation of the laser over a diffuse scattering POM window can be reconstructed with sufficient accuracy using SMI by applying the theory outlined in Sec. 2.1.

In vivo experiments are required to determine the influence of speckle on the Doppler signals when measuring on real skin. Moreover, during *in vivo* experiments the laser diode will move more irregularly with respect to the skin, during which the distance L_o between the laser diode and the skin will vary over time as well. The variation of this distance can also adversely affect the amplitude of the Doppler signals [Eqs. (8) and (10)]. Furthermore, in this case the displacement can no longer be measured in absolute units, because a three-dimensional motion is projected onto a single axis.

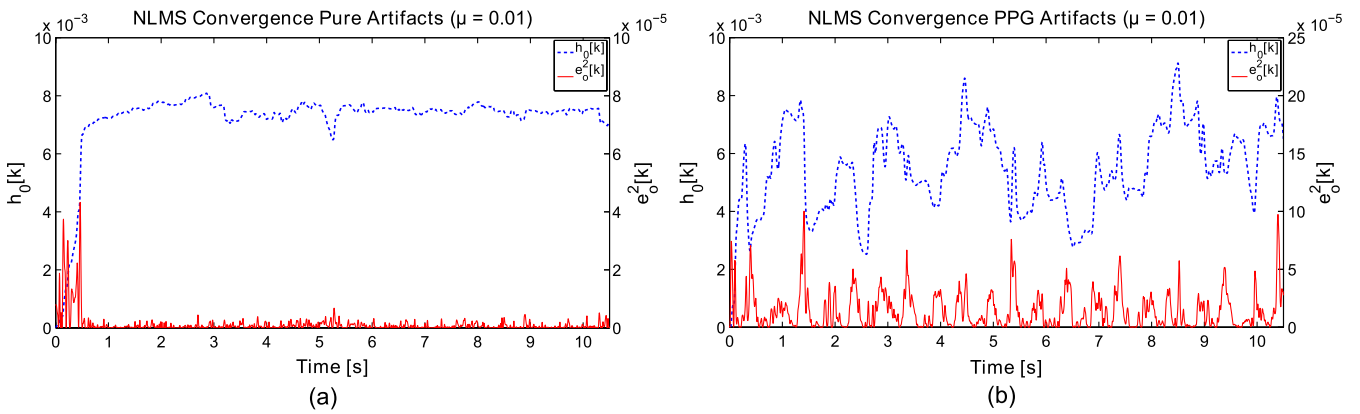

Fig. 13 Convergence of the NLMS algorithm. The dashed and solid curves show the convergence of the filter weight $h_0[k]$ and the output power $e_o^2[k]$, respectively. (a) Convergence for pure artifacts. (b) Convergence for artifacts corrupting a PPG.

4.2 *Measuring In Vitro PPGs*

Although the channel is rigid, the weak PPG measured in case 1 [solid curve in Fig. 11(a)] is still a result of the increase in milk volume in the channel. Milk volume increases in this channel because of upward deflection of the window, thus increasing the amount of backscattered light that reaches the detector.

When comparing case 2 to case 1, the PPG waveform is more smooth and its amplitude increases by a factor of 2.4, while the window deflection decreases by a factor of 2.4 [Fig. 11(b)]. The upward motion of the window decreases, because the increased channel compliance decreases the pressure in the channel. Furthermore, the silicone membranes cause the periodic increases in channel volume to be larger compared to the rigid channel. And as in case 1, the PPG is in phase with the window deflection. Therefore, it is concluded that the increased PPG amplitude has to be attributed to the stronger backscattering as a result of the larger increase in milk volume in the flexible channel. Furthermore, in this case the PPG's DC level has increased by approximately 100 mV, because light reaches the detector that has tunneled through the silicone membrane and possibly has been reflected back from the base, as indicated by the third and fourth term in Eq. (26). These light paths contribute to the increased PPG amplitude as well. However, because the PPG amplitude is mostly a result of increased backscattering in the milk, the most direct paths via the milk volume will provide the largest contribution to the PPG pulse.

When using milk as a blood phantom, the PPG amplitude is in phase with the deflection of the window, i.e., an increase in milk volume leads to an increase in the PPG. This is opposite to most *in vivo* reflectance PPGs, which show a decrease upon an increase in blood volume, as a result of increased absorption.[10,46] In case 3, a PPG is measured of which the amplitude is in antiphase with window deflection [Fig. 11(c)], i.e., as a result of the added absorption, an increase in milk volume now does lead to a decrease in the PPG. Furthermore, the resulting PPG has a relative amplitude of 4%, which is comparable to the relative amplitude of *in vivo* PPGs.[2,5,14] Therefore, it is concluded that in case 3 an *in vitro* PPG representative of *in vivo* PPGs is obtained by adding a water-soluble black dye to the milk. Lastly, deflection of the window observed *in vitro* is considered a relevant effect, because skin pulsates *in vivo* as a result of pulsations of the arterial blood.

In the perfusion phantom, a small laser displacement of 100 to 200 μm results in optical motion artifacts with a magnitude comparable to the PPG magnitude [Fig. 12(b)]. However, the skin perfusion phantom only models the basic optical effects qualitatively. It is for instance not known whether the optical shunt through the POM window has a realistic contribution to the measured PPG. Therefore, no conclusion can be drawn from the *in vitro* model regarding the magnitude of motion artifacts expected *in vivo* as a result of relative sensor motion.

Finally, the measurements with pure milk illustrate the limitations of the Beer-Lambert model for strongly scattering media.[2,46] Increases in detected light intensity caused by increases in milk volume result from an increased light scattering [Fig. 11(a) and 11(b)]. This effect cannot be described by the Beer-Lambert law, which only takes into account light absorption. Therefore, it should be noted that the model proposed in Sec. 2.3.1 can only be interpreted as an approximate description of the detected light intensity.

4.3 *Motion Artifact Reduction*

Figure 12(a) and 12(b) shows that the optical motion artifacts are in phase with the laser displacement, i.e., when the laser moves towards the PPG photodiode (positive displacement), the measured light intensity increases. This is in correspondence with the Taylor approximation of the PPG signal in Eq. (27): a decrease in emitter-detector distance increases the light intensity received. Figure 12(a) and 12(b) furthermore show a significant reduction of optical motion artifacts via an NLMS algorithm that adaptively scales the laser displacement to estimate the artifacts. This indicates a strong correlation between the laser displacement and the artifacts, thus confirming our hypothesis *in vitro*. The fast convergence in Fig. 13 indicates feasibility of a real-time implementation.

Figure 12(a) and 12(b) also illustrates that the proposed algorithm does not fully suppress the motion artifacts. This is a result of fast fluctuating artifacts which are beyond the adaptation speed of the algorithm. Increasing step-size parameter μ would increase the adaptation speed, but this cannot be done to assure stability. Furthermore, the pure motion artifact in Fig. 12(a) shows fast fluctuations which are not present in the displacement in Fig. 12(c), e.g., at 0.3 s. These fast fluctuations are a result of small inhomogeneities in the skin perfusion phantom and are multiplicative effects on the pure displacement artifact. Because visual inspection of the monitor diode's DC level shows that the laser's optical output power remains constant during motion, it can be concluded that these fast fluctuations are not the result of fluctuations in the optical power. Also these multiplicative artifacts as a result of inhomogeneities have not been estimated accurately, because they are beyond the adaptation speed of the algorithm. In addition, the NLMS algorithm may have to correct for the inaccuracies in the SMI displacement measurement as a result of speckle. This would be done by adjusting $h_0[k]$, which slows down the process of estimating the motion artifacts. Moreover, Fig. 12(a) and 12(b) shows that artifacts in a corrupted PPG are suppressed to a smaller extent compared to pure artifacts. In part, this is caused by the influence of the PPG in $e_o[k]$ on the adaptation of $h_0[k]$, as shown in Fig. 13. In case of the corrupted PPG, $h_0[k]$ fluctuates strongly over time, as a result of the fact that $e_o[k]$ also contains the PPG and the cross-correlation in the weight update rule [Eq. (29)]. Additionally, the reduction in performance is attributed to the fact that the deflection of the window is measured via SMI, as shown by $\Delta L_{\mathrm{err}}(t)$ [thin curve in Fig. 12(d)], which is correlated to the PPG. Because the NLMS algorithm is a correlation canceler, the window deflection component in the SMI measurement can affect the PPG.

In vivo measurements are necessary to determine the true potential of the proposed method. In this case, SMI with one laser diode will provide a one-dimensional reference of three-dimensional sensor-tissue motion. The usefulness of such a reference is to be determined. Furthermore, more complex motion artifacts will be observed in the PPGs, which presumably result from optical coupling effects, sloshing of blood and deformation of the skin. *In vivo* results will demonstrate whether sensor-tissue motion as measured via SMI correlates to other artifacts than optical artifacts as well. Lastly, it is likely that pulsations of the skin at the pulse rate will be measured via SMI, which can affect the PPG when removing motion artifacts based on correlation cancellation. Furthermore, as the laser light will be focused onto the skin, it is expected that the contribution of laser light directly backscattered by the pulsating skin will

dominate the contribution of laser light backscattered by the randomly moving red blood cells in the dermis. Therefore, it is expected that the components in the relative motion signal which directly result from moving red blood cells are negligible.

5 Conclusions

It has been hypothesized that optical motion artifacts in a PPG as a result of sensor motion or deformation correlate with movement of the emitter with respect to the skin. This hypothesis has been proven true in a laboratory setup. *In vitro* PPGs have been measured in a skin perfusion phantom that is illuminated by a laser diode. Optical motion artifacts are generated in the PPG by translating the laser diode with respect to the PPG photodiode. It has been shown that a significant reduction of the optical motion artifacts can be achieved *in vitro* using an NLMS algorithm with only a single coefficient, that uses the laser's displacement as a reference for the motion artifacts. Furthermore, it has been shown that laser displacement can be measured accurately via SMI by a compact laser diode with a ball lens integrated into the package, which can be easily integrated into a commercial sensor. Promising results have been obtained using the *in vitro* setup. *In vivo* measurements now have to be performed to determine the true potential of the use of sensor displacement as a means to reduce motion artifacts in PPGs.

Acknowledgments

This work was supported by NL Agency, IOP Photonic Devices, IPD083359 HIP—Hemodynamics by Interferometric Photonics. The skin perfusion phantom has been developed by HemoLab cardiovascular engineering, Eindhoven, the Netherlands. The authors are very grateful to Mr. Ben Wassink of VDL ETG Research bv, for his great efforts in designing and constructing the experimental setup. The authors are also grateful to Dr. Martin van der Mark of Philips Research for his advice on light-tissue interaction and the construction of the skin perfusion phantom. Finally, the authors like to thank Mr. Henny Herps for the drawing of the finger with the pulse oximetry clip.

References

1. M. T. Petterson, V. L. Begnoche, and J. M. Graybeal, "The effect of motion on pulse oximetry and its clinical significance," *Anesth. Analg.* **105**(6S Suppl), S78–S84 (2007).
2. P. D. Mannheimer, "The light-tissue interaction of pulse oximetry," *Anesth. Analg.* **105**(6S Suppl), S10–S17 (2007).
3. J. G. Webster, Ed., *Design of Pulse Oximeters*, Taylor & Francis Group, New York (1997).
4. J. Allen, "Photoplethysmography and its application in clinical physiological measurement," *Physiol. Meas.* **28**(3), R1–R39 (2007).
5. R. D. Branson and P. D. Mannheimer, "Forehead oximetry in critically ill patients: the case for a new monitoring site," *Resp. Care Clin. N. Am.* **10**(3), 359–367 (2004).
6. S. J. Choi et al., "Comparison of desaturation and resaturation response times between transmission and reflectance pulse oximeters," *Acta Anaesth. Scand.* **54**(2), 212–217 (2010).
7. Y. Yamaya et al., "Validity of pulse oximetry during maximal exercise in normoxia, hypoxia, and hyperoxia," *J. Appl. Physiol.* **92**(1), 162–168 (2002).
8. J. Muehlsteff et al., "Phase-space representation of photoplethysmography signals as visualization concept," in *Proc. BMT 2010, 44. Jahrestagung der Deutschen Gesellschaft für Biomedizinische Technik*, De Gruyter, Rostock, Germany (2010).
9. W. B. Murray and P. A. Foster, "The peripheral pulse wave: information overlooked," *J. Clin. Monitor.* **12**(5), 365–377 (1996).
10. A. Reisner et al., "Utility of the photoplethysmogram in circulatory monitoring," *Anesthesiology* **108**(5), 950–958 (2008).
11. K. H. Shelley, "Photoplethysmography: beyond the calculation of arterial oxygen saturation and heart rate," *Anesth. Analg.* **105**(6S Suppl), S31–S36 (2007).
12. P. S. Addison et al., "Developing an algorithm for pulse oximetry derived respiratory rate (RR_{oxi}): a healthy volunteer study," *J. Clin. Monitor. Comp.* **26**(1), 45–51 (2012).
13. S. Lu et al., "Can photoplethysmography variability serve as an alternative approach to obtain heart rate variability information?," *J. Clin. Monitor. Comp.* **22**(1), 23–29 (2008).
14. M. Nitzan et al., "The variability of the photoplethysmographic signal—a potential method for the evaluation of the autonomic nervous sytem," *Physiol. Meas.* **19**(1), 93–102 (1998).
15. O. Such and J. Muehlsteff, "The challenge of motion artifact suppression in wearable monitoring solutions," in *Proc. 3rd IEEE-EMBS International Summer School and Symposium on Medical Devices and Biosensors*, pp. 49–52, IEEE, Boston (2006).
16. S. Kaestle, H. Block, and M. Block, "Method and apparatus for determining the concentration of a component," U. S. Patent No. 6,122,535 (2000).
17. S. Kästle, "Recognition of a useful signal in a measurement signal," U. S. Patent No. 6,631,281 B1 (2003).
18. J. M. Goldman et al., "Masimo signal extraction pulse oximetry," *J. Clin. Monitor. Comp.* **16**(7), 475–483 (2000).
19. M. K. Diab et al., "Signal processing apparatus," U. S. Patent No. 6,745,060 B2 (2004).
20. H. H. Asada et al., "Mobile monitoring with wearable photoplethysmographic biosensors," *IEEE Eng. Med. Biol. Mag.* **22**(3), 28–40 (2003).
21. L. Wang, B. P. L. Lo, and G.-Z. Yang, "Multichannel reflective PPG earpiece sensor with passive motion cancellation," *IEEE Trans. Biomed. Circ. Syst.* **1**(4), 235–241 (2007).
22. B. Lee et al., "Improved elimination of motion artifacts from a photoplethysmographic signal using a Kalman smoother with simultaneous accelerometry," *Physiol. Meas.* **31**(12), 1585–1603 (2010).
23. P. T. Gibbs, L. B. Wood, and H. H. Asada, "Active motion artifact cancellation for wearable health monitoring sensors using collocated MEMS accelerometers," *Proc. SPIE* **5765**, 811–819 (2005).
24. M. J. Hayes and P. R. Smith, "A new method for pulse oximetry possessing inherent insensitivity to artifact," *IEEE Trans. Biomed. Eng.* **48**(4), 452–461 (2001).
25. P. S. Addison and J. N. Watson, "Oxygen saturation determined using a novel wavelet ratio surface," *Med. Eng. Phys.* **27**(3), 245–248 (2005).
26. Y.-S. Yan, C. C. Y. Poon, and Y.-T. Zhang, "Reduction of motion artifact in pulse oximetry by smoothed pseudo Wigner-Ville distribution," *J. Neuroeng. Rehabil.* **2**(3) (2005).
27. T. Aoyagi et al., "Multiwavelength pulse oximetry: theory for the future," *Anesth. Analg.* **105**(6S Suppl), S53–S58 (2007).
28. R. W. C. G. R. Wijshoff et al., "PPG motion artifact handling using a self-mixing interferometric sensor," *Proc. SPIE* **7894**, 78940F (2011).
29. S. Haykin, *Adaptive Filter Theory*, T. Kailath, Ed., Information and System Sciences Series, Prentice-Hall, Upper Saddle River, NJ (1996).
30. K. Petermann, *Laser Diode Modulation and Noise*, Kluwer Academic Publishers, Dordrecht (1988).
31. G. A. Acket et al., "The influence of feedback intensity on longitudinal mode properties and optical noise in index-guided semiconductor lasers," *IEEE J. Quantum Electron.* **20**(10), 1163–1169 (1984).
32. G. Giuliani et al., "Laser diode self-mixing technique for sensing applications," *J. Opt. A- Pure Appl. Opt.* **4**(6), S283–S294 (2002).
33. M. H. Koelink et al., "Laser Doppler velocimeter based on the self-mixing effect in a fiber-coupled semiconductor laser: theory," *Appl. Opt.* **31**(18), 3401–3408 (1992).
34. P. J. de Groot, G. M. Gallatin, and S. H. Macomber, "Ranging and velocimetry signal generation in a backscatter-modulated laser diode," *Appl. Opt.* **27**(21), 4475–4480 (1988).
35. D. Guo and M. Wang, "Self-mixing interferometry based on a double-modulation technique for absolute distance measurement," *Appl. Opt.* **46**(9), 1486–1491 (2007).
36. A. Cuyt et al., *Handbook of Continued Fractions for Special Functions*, Springer, Berlin (2008).
37. L. R. Rabiner and B. Gold, *Theory and Application of Digital Signal Processing*, Prentice-Hall, Englewood Cliffs, NJ (1975).
38. U-L-M Photonics, "850 nm VCSEL," http://www.ulm-photonics.com/.
39. P. Agache and P. Humbert, Eds., *Measuring the Skin*, Springer, Berlin (2004).

40. I. M. Braverman, "The cutaneous microcirculation," *J. Invest. Dermatol. Symposium Proc.* **5**(1), 3–9 (2000).
41. J. L. Reuss and D. Siker, "The pulse in reflectance pulse oximetry: modeling and experimental results," *J. Clinical Monitor. Comp.* **18**(4), 289–299 (2004).
42. M. Vegfors et al., "Accuracy of pulse oximetry at various haematocrits and during haemolysis in an *in vitro* model," *Med. Biol. Eng. Comput.* **31**(2), 135–141 (1993).
43. R. Lohwasser and G. Soelkner, "Experimental and theoretical laser-Doppler frequency spectra of a tissuelike model of a human head with capillaries," *Appl. Opt.* **38**(10), 2128–2137 (1999).
44. A. C. Guyton and J. E. Hall, *Textbook of Medical Physiology*, Saunders, Philadelphia (2000).
45. M.-C. Michalski, V. Briard, and F. Michel, "Optical parameters of milk fat globules for laser light scattering measurements," *Lait* **81**(6), 787–796 (2001).
46. R. Graaff et al., "How tissue optics influences reflectance pulse oximetry," *Adv. Exp. Med. Biol.* **388**, 117–132 (1996).
47. J. Qin and R. Lu, "Measurement of the absorption and scattering properties of turbid liquid foods using hyperspectral imaging," *Appl. Spectrosc.* **61**(4), 388–396 (2007).